Supplementary Text S1 LSTM prediction models of GPP and ET

This study employs long short-term memory (LSTM) networks for flux modeling, leveraging their advanced deep learning architecture that is particularly suited for capturing complex temporal dynamics. The LSTM approach has been demonstrated as effective for GPP prediction [64] and ET estimation [65] in previous research. Through an iterative training and validation process, we optimized the model hyperparameters, with detailed configurations provided in Table S1.

Table S1. Hyperparameters of long short-term memory model used in the present study.

Module	Layer/Parameter	Value	Input Shape	Output Shape	Description
Input Layer	-	-	(batch, 30, 14)	-	14 features, 30-day time steps
LSTM Layer	num_layers=4	4	(batch, 30, 14)	(batch, 30, 128)	4 stacked LSTMs, 128 hidden units (returns all time steps), 30% dropout between layers (except last layer)
	hidden_size=128	128			
	dropout=0.3	0.3			
Dropout Layer	p=0.3	0.3	(batch, 30, 128)	(batch, 30, 128)	30% neuron dropout before output
Linear Layer	in=128, out=1	Linear(128,1)	(batch, 30, 128)	(batch, 30, 1)	Maps 128-dim features to NEE predictions
Training	batch_size	128	-	-	Samples per batch
	learning_rate	0.001	-	-	Initial Adam optimizer learning rate
	min_learning_rate	0.0001	-	-	Minimum learning rate for decay
	epochs	50	-	-	Maximum training epochs
	patience	10	-	-	Early stopping patience (epochs)

Ecosystem carbon–water fluxes are shaped by multiple environmental drivers, such as climate, CO_2 fertilization, land-use change, nitrogen deposition, and soil properties [66–68]. As a sensitive indicator of ecosystem function, the LAI integrates the effects of land-use transitions, CO_2-driven photosynthesis, and nitrogen-enhanced biomass [69–71]. Combining a high-resolution LAI with meteorological data, machine learning models can reveal nonlinear vegetation–environment relationships, thereby improving the mechanistic understanding of carbon flux variability [72,73]. Based on GPP and ET data from daily flux stations, combined with predictors from multiple sources (Table S2), a daily-scale GPP and ET simulation model based on LSTM was constructed and trained. The predictive factors used include TMAX, TMEAN, TMIN, VPD, WIND, LAI, downward

shortwave radiation (DSR), topsoil (0-30 cm) clay fraction (CLAY), topsoil sand fraction (SAND), and topsoil soil carbon fraction (SOCD). The LAI data were derived from MOD15A3H products and temporally interpolated to daily resolution. DSR data were obtained from MCD18A1 products. Soil properties were extracted from the Harmonized World Soil Database (HWSD). Using the Google Earth Engine platform, we extracted values for all variables within a 500-meter radius buffer surrounding each flux tower (and meteorological station) location.

Table S2. Summary of model variables.

Name	Description	Unit	Temporal/Spatial resolution	Source
TMAX	Maximum air temperature	°C	Daily	GSOD
TMIN	Minimum air temperature	°C	Daily	
TMEAN	Mean air temperature	°C	Daily	
WIND	Wind speed	m/s	Daily	
VPD	Vapor pressure deficiency	kPa	Daily	
LAI	Leaf area index	m^2/m^2	4-day/500m	MOD15A3H
DSR	Downward shortwave radiation	w/m^2	Daily/1000m	MCD18A1
CLAY	Topsoil (0-30 cm) clay fraction	%	Static	HWSD V2.0
SAND	Topsoil (0-30 cm) sand fraction	%	Static	
SOCD	Topsoil (0-30 cm) soil carbon fraction	%	Static	

2. Spatial and temporal variation attribution of GPP and ET and their response to drought

This study utilized the constructed LSTM model to simulate daily-scale GPP and ET data from 684 corn-growing meteorological stations in the COUNS. Based on the criterion that monthly observation data exceeded 25 days, summer data from June to August were extracted. To further analyze the response mechanisms of corn ecosystems under extreme drought conditions, 136 stations with observation records from 2012 were selected, with a focus on examining the spatiotemporal characteristics of GPP and ET during drought years and their differences from those in normal years.

To evaluate maize ecosystem responses to this extreme drought event, we calculated the difference between ET and precipitation (ET-PRE) as an indicator of potential contributions from either irrigation inputs or deep soil water extraction to evapotranspiration. In addition, photosynthetic efficiency per unit leaf area (GPP/LAI) and water use efficiency (GPP/ET) are used as indicators of whether crops have increased their carbon fixation capacity per unit leaf area, whether the distribution strategy of photosynthetic products has been adjusted under drought conditions, and whether water use efficiency has been enhanced. We compare the key response indicators of each site in 2012 with those of other years to reveal the changing characteristics of the simulated meteorological station cornfield ecosystem's adaptation to extreme drought. To thoroughly analyze the response mechanisms of GPP and ET to key environmental factors, this paper uses partial correlation analysis to measure the independent contribution of target factors to the carbon–water process while controlling for interference by other variables.

Supplementary Text S2 Data Processing

1. Flux station data and meteorological station data

The flux station observation data used for model training are sourced from the FLUXNET2015 and Ameriflux datasets (Table S3). GPP (gC m^{-2} d^{-1}) was obtained from the field GPP_NT_VUT_REF, while ET (mm d^{-1}) was derived by multiplying the latent heat flux LE (W m^{-2}) by a conversion factor of 0.03527. The dataset also includes daily meteorological variables such as maximum air temperature (TMAX), minimum air temperature (TMIN), mean air temperature (TMEAN), wind speed (WIND), and vapor pressure deficit (VPD). The data preprocessing pipeline consisted of: (1) quality control of GPP and ET records across all sites, retaining only high-quality observations with QC values >0.75 to ensure data reliability [74]; (2) removal of records containing significant outliers or missing key explanatory variables [75]; (3) exclusion of pre-2000 observations to maintain temporal consistency with remote sensing products; and (4) selection of observations from maize cultivation years. After these filtering steps, 17 maize flux tower stations (Fig. 2) were ultimately retained for training machine learning models to simulate GPP and ET.

The meteorological data were obtained from the Global Surface Summary of the Day (GSOD) [https://catalog.data.gov/dataset/global-surface-summary-of-the-day-gsod], which provides daily weather observations from tens of thousands of meteorological stations (Fig. 2), including TMAX, TMIN, TMEAN, WIND, and relative humidity (RH). VPD was calculated from TMEAN and RH. To ensure consistency between meteorological station data and flux tower measurements, identical data quality screening criteria were applied. This study specifically focuses on analyzing ecological response characteristics during the maize growing season (June – August), with additional filtering for periods when the leaf area index (LAI) is greater than 0.3. After applying all quality controls, a total of 684 stations were retained for generating GPP and ET estimates.

2. Other data

The 1 km resolution annual maize distribution data were obtained from the Cropland Atlas of the United States (CropAT-US) [29]. For post-2000 records, the dataset primarily integrates farmland spatial information derived from four remote sensing products with three historical inventory surveys through a Bayesian fusion modeling approach. The simulated maize acreage demonstrates strong consistency with county-level statistics, with correlation coefficients generally exceeding 0.95, confirming its suitability for agricultural research and flux modeling applications. This dataset was principally employed to identify maize cultivation years for each flux tower and meteorological station.

We employed the reanalysis dataset TerraClimate to characterize large-scale drought patterns [30], which features 4 km spatial resolution. TerraClimate reconstructs high-resolution monthly climate records since 1958 by integrating multi-source data including CRU Ts4.0, JRA55, and WorldClim. For our comparative analysis with meteorological station observations, we extracted the following variables: precipitation (PRE), TMAX, TMIN, TMEAN, VPD, and WIND.

Table S3. Summary of flux sites in corn ecosystem.

ID	Longitude	Latitude	Length	Period
US-Twt	-121.6531	38.1087	1096	2012-2014
US-Tw3	-121.6469	38.1152	2205	2013-2018

US-Bi2	-121.5351	38.1091	1131	2017-2021
US-Ne1	-96.4766	41.1651	4018	2001-2013
US-Ne2	-96.4701	41.1649	4018	2001-2013
US-Ne3	-96.4397	41.1797	2555	2001-2013
US-Ro1	-93.0898	44.7143	2051	2005-2015
US-Ro2	-93.0888	44.7288	1149	2008-2016
US-Ro6	-93.0578	44.6946	653	2018-2020
US-Ro5	-93.0576	44.691	719	2017-2019
US-Mo3	-92.1497	39.2311	1047	2017-2021
US-Mo1	-92.1167	39.2298	798	2015-2021
US-RGA	-91.6733	34.4159	249	2021-2021
US-DFC	-89.7117	43.3448	335	2019-2019
US-CS3	-89.5727	44.1394	124	2020-2020
US-CS1	-89.5379	44.1031	177	2018-2018
US-CRT	-83.3471	41.6285	704	2011-2011

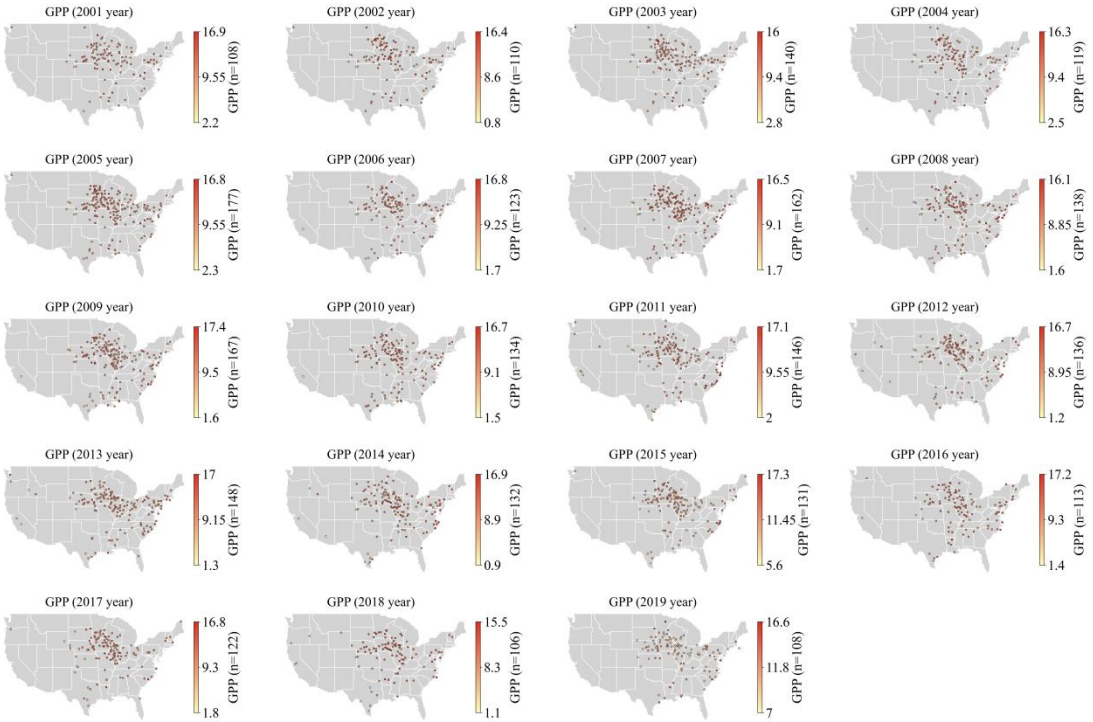


Figure S1. Annual GPP distribution for corn meteorological stations.

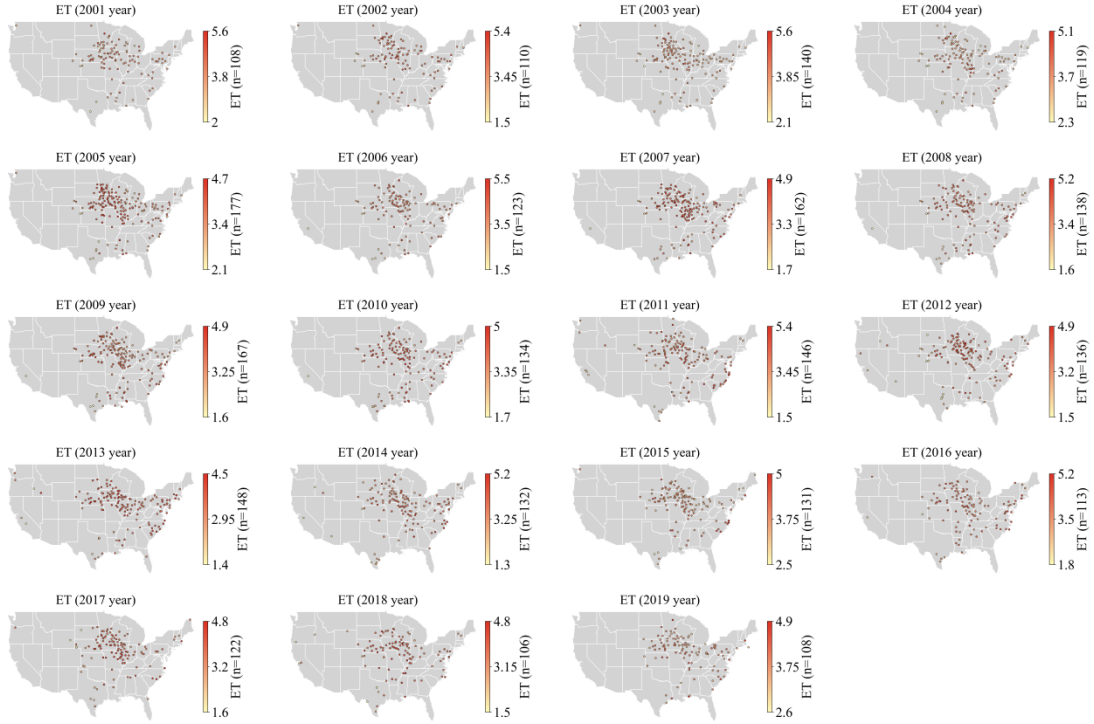


Figure S2. Annual ET distribution for corn meteorological stations.

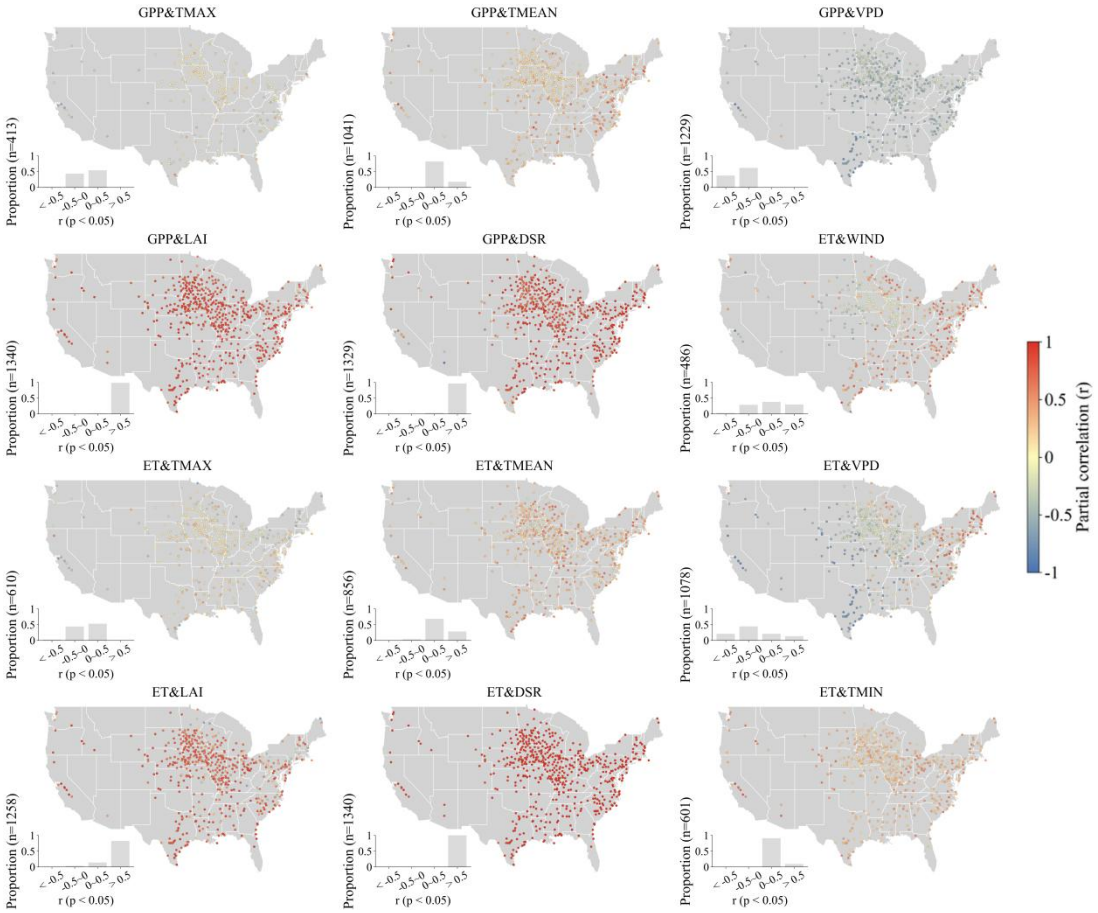


Figure S3. Spatial distribution maps of partial correlation coefficients between daily GPP and ET at each site during summer and environmental variables. Only sites with significance levels $p<0.05$ are shown.

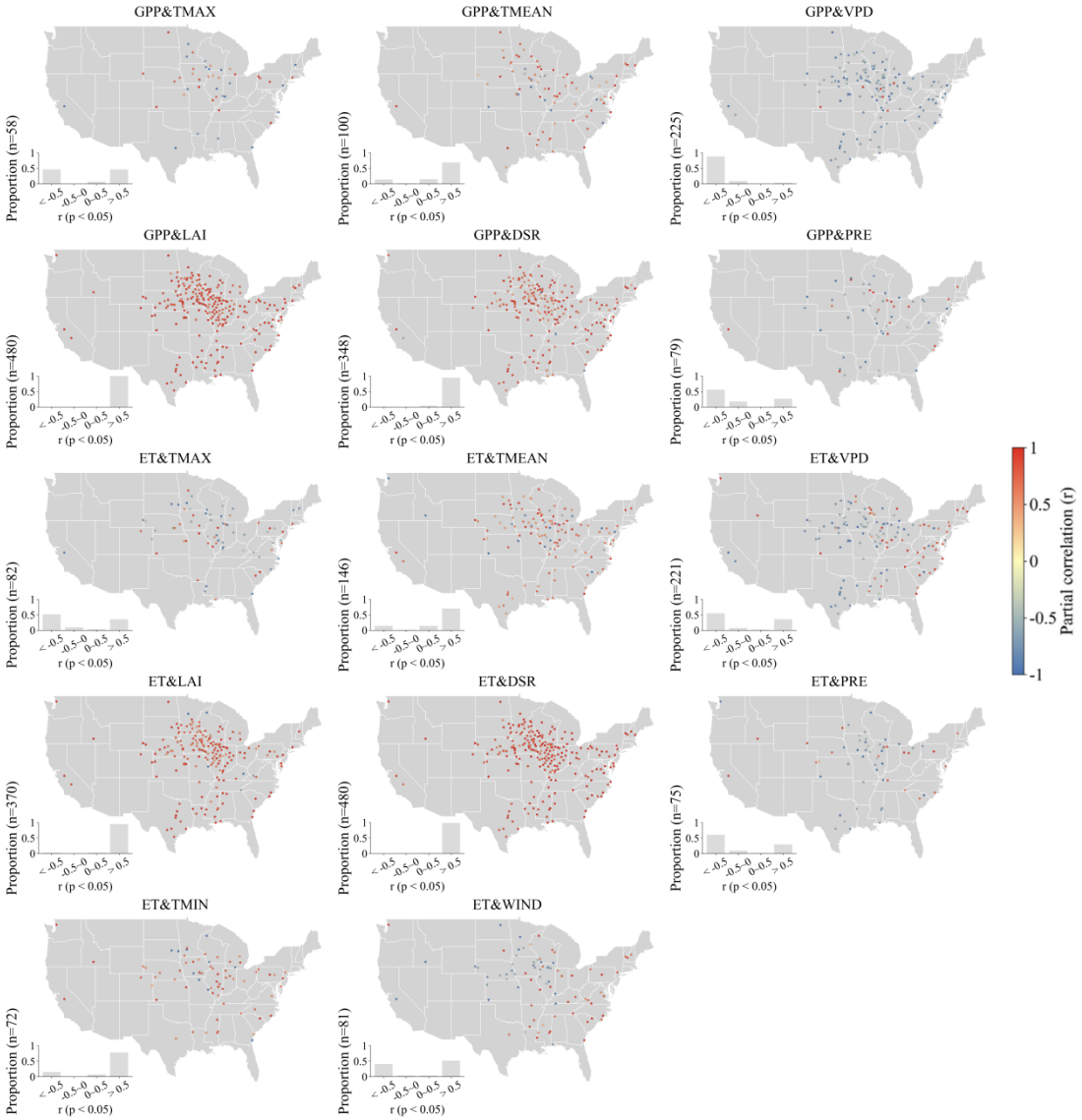


Figure S4. Spatial distribution maps of partial correlation coefficients between monthly GPP and ET at each site during summer and environmental variables. Only sites with significance levels $p<0.05$ are shown.

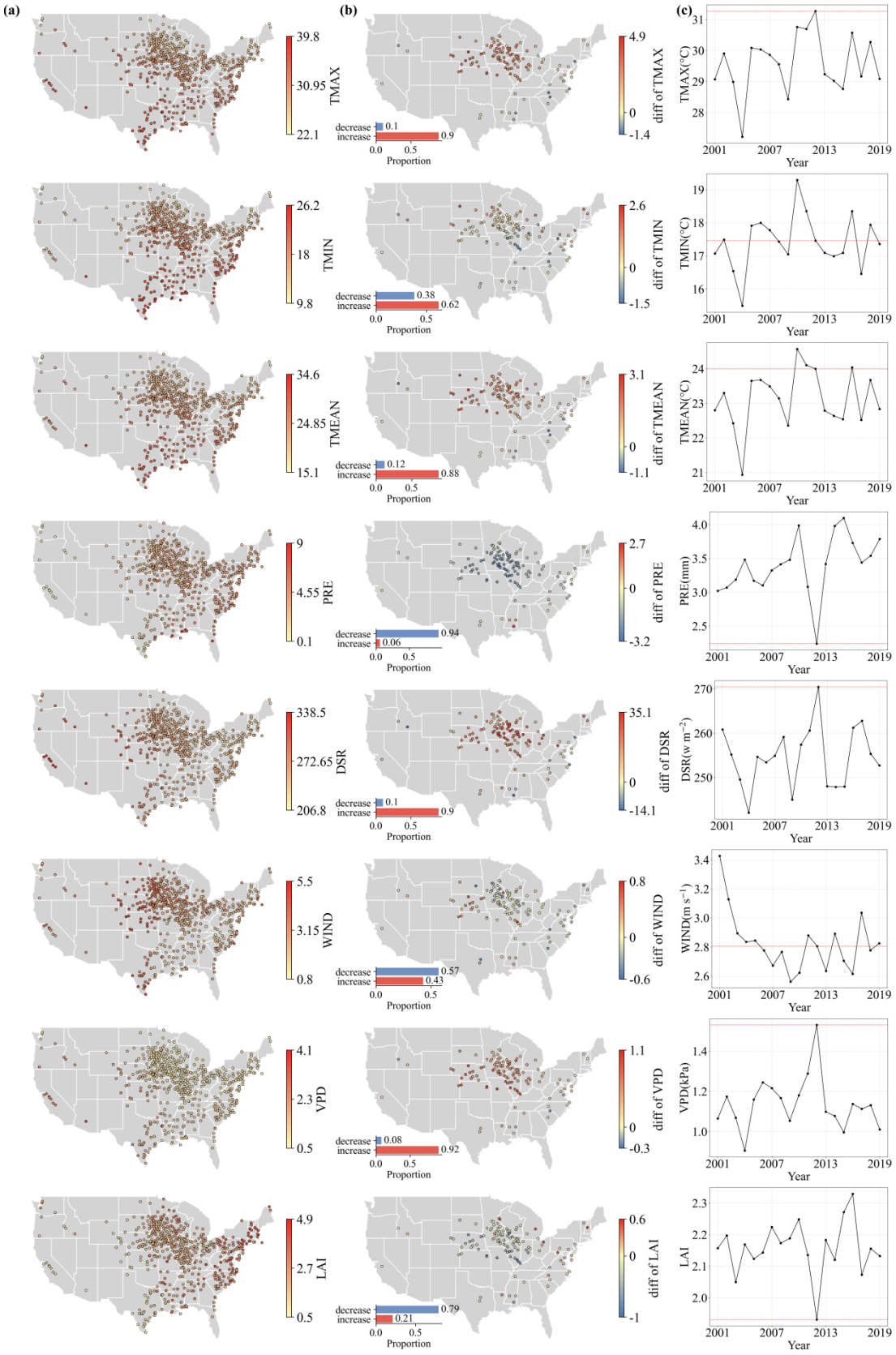


Figure S5. Differences between the long-term summer averages of variables at meteorological stations and the extreme drought event of 2012. (a) Multi-year summer averages of variables at each site, except for 2012. (b) Spatial distribution map of the differences between the 2012 summer mean values of each variable and the long-term summer average values; red areas indicate that the 2012 summer values at that location were higher than the long-term summer average values (difference

> 0); blue areas indicate that the 2012 summer values at that location were lower than the long-term summer average values (difference < 0). (c) Interannual trend, with the red line representing 2012.

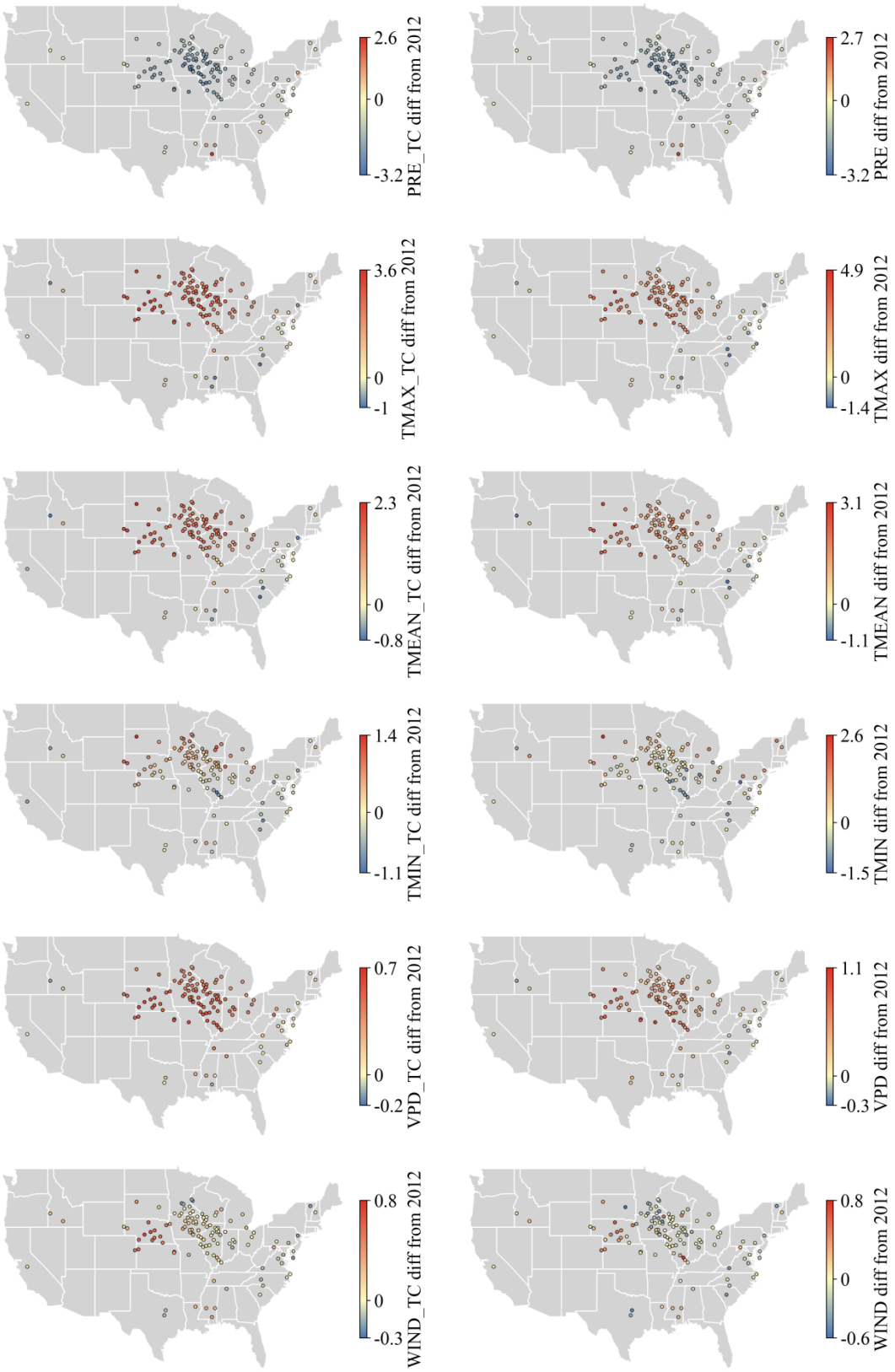


Figure S6. Comparison of the multi-year average values of meteorological variables at various stations during summer with the anomalies in 2012: (a) results from remote sensing product inversion; (b) meteorological station observation data.